3d printed continuous fiber reinforced composite auxetic honeycomb structures

Chao Quan [a,b,c], Bin Han [b,d,e,*], Zhanghao Hou [f], Qi Zhang [b,d], Xiaoyong Tian [f], Tian Jian Lu [c,g,**]

[a] State Key Laboratory for Strength and Vibration of Mechanical Structures, Xi'an Jiaotong University, Xi'an, 710049, China
[b] School of Mechanical Engineering, Xi'an Jiaotong University, Xi'an, 710049, China
[c] State Key Laboratory of Mechanics and Control of Mechanical Structures, Nanjing University of Aeronautics and Astronautics, Nanjing, 210016, China
[d] National Innovation Institute of Additive Manufacturing, Xi'an, 710000, China
[e] Research Institute of Xi'an Jiaotong University, Zhejiang, Hangzhou, 311215, China
[f] State Key Laboratory for Manufacturing Systems Engineering, Xi'an Jiaotong University, China
[g] Nanjing Center for Multifunctional Lightweight Materials and Structures (MLMS), Nanjing University of Aeronautics and Astronautics, Nanjing, 210016, China

ARTICLE INFO

ABSTRACT

Continuous fiber reinforced thermoplastic composite (CFRTPC) auxetic honeycomb structures were fabricated using the 3D printing technology with a specific printing path planning. For comparison, auxetic honeycombs were also fabricated with pure polylactic acid (PLA). In-plane compression tests were conducted, with corresponding damage types explored using Scanning Electron Microscopy (SEM) images. A printing path-based finite element (FE) method was developed to mimic both small and large deformations of CFRTPC auxetic honeycombs, while analytical model was proposed to predict their effective stiffness and Poisson ratio. Good agreement was achieved among analytical predictions, FE simulation results and experimental measurements. A systematic parametric study was subsequently carried out to quantify the dependence of in-plane mechanical properties on geometrical parameters. Compared with pure PLA structures, the presence of continuous fibers efficiently prohibited crack propagation in the matrix for each ligament of CFRTPC auxetic honeycombs. Adding continuous fibers increased the mass only by 6%, but led to dramatic increase in compressive stiffness and energy absorption by 86.3% and 100% respectively and smaller Poisson ratios. The proposed 3D printing technology has great potential in integrated fabrication of continuous fiber reinforced composite lightweight structures having complex shapes, attractive mechanical properties, and multifunctional attributes.

1. Introduction

Altering the cell angles of a hexagonal honeycomb could enable the structure to exhibit negative Poisson ratio [1], also called the auxetic effect. Typically, auxetic honeycombs contract (expand) transversely when compressed (stretched) in axial direction. Further, auxetic structures possess superior mechanical and physical properties as compared with conventional structures, e.g., increased shear modulus, indentation resistance, fracture toughness, energy absorption, strain-dependent porosity/permeability, and synclastic curvature. While such auxetic structures have long existed in nature, since 1980s people have begun to design and manufacture foams [2–4], polymeric materials [5–7] and composite materials [8–11] with negative Poisson ratios. More recently,

a multitude of two-dimensional (2D) [12–18] and three-dimensional (3D) [19–23] structures made of various parent materials, which exhibit auxetic behaviors under multiple loading conditions, have been developed.

Along separate but distinct development routes, fiber reinforced composite lightweight structures (FRCLSs) extract extensive research interests due to their high specific strength and specific stiffness, good thermal stability, well design flexibility, recycling and easy machining. Several conventional processes have been developed to fabricate the FRCLSs, including interlock assembly molding [24], filament knitting [25], hot press molding [26,27] and vacuum assisted resin infusion [28]. However, these methods are often complicated, costly and time-consuming. In addition, widespread industrial applications of

---

* Corresponding author. School of Mechanical Engineering, Xi'an Jiaotong University, Xi'an, 710049, China.
** Corresponding author. State Key Laboratory of Mechanics and Control of Mechanical Structures, Nanjing University of Aeronautics and Astronautics, Nanjing, 210016, China.

E-mail addresses: hanbinghost@xjtu.edu.cn (B. Han), tjlu@nuaa.edu.cn (T.J. Lu).

FRCLSs are limited by the use of mould and low degree of automation.

Different from the conventional fabrication approaches, 3D printing based fabrication of continuous fiber reinforced thermoplastic composites (CFRTPCs) has become a new manufacturing method, with relatively short production cycle, low cost and high degree of automation. It not only promotes integrated forming of complex structural parts but also provides an effective approach for low-cost rapid manufacturing of continuous FRCLSs [29,30]. For instance, an innovative technique for in-nozzle impregnation of continuous fiber and thermoplastic matrix was developed [31], and the effects of temperature and extrusion nozzle pressure on the mechanical properties of 3D printed continuous carbon fiber reinforced PLA (polylactic acid) composites were systematically studied [32]. Further, the mechanical properties of the printed composites with or without preprocessed carbon fiber bundles were compared [33], and the performances of continuous carbon, Kevlar and glass fiber reinforced Nylon composites fabricated using a Markforged Mark One 3D printing system were evaluated [34]. The effect of build orientation, layer thickness and fiber volume content on the interlaminar bonding, impact and mechanical performance were evaluated utilizing short beam shear, charpy impact, tensile and three-point bending tests, respectively [35–37]. Subsequently, a new 3D printer equipped with a novel nozzle structure which can supply continuous carbon fiber reinforced thermoplastics filaments and additional matrix resin independently was developed [38].

To further reduce the weight of FRCLSs, 3D printed prismatic and lattice structures have been developed [39–41]. Hou et al. [39] prepared CFRTPC corrugated structures using the 3D printing technology, and explored the effects of printing parameters on fiber content and mechanical properties. Liu et al. [40] studied the compression performance of printed CFRTPC pyramid lattice structures, and found that the existence of many voids caused by the lack of pressure during printing led to poor mechanical properties of the structure. Further, the functional properties of printed CFRTPC honeycomb, rhombus, rectangle and circle sandwich structures were investigated using shape evaluations and three-point bending tests [41]. At present, however, there were few reports concerning auxetic CFRTPC honeycombs prepared via 3D printing. In addition, as existing 3D printed continuous FRCLSs were all fabricated based upon the specific one-stroke printing path, it is

necessary to develop printing path-based analytical or numerical modelling of 3D printed CFRTPC structures.

In this study, a group of auxetic honeycombs made of CFRTPC and pure PLA were designed and fabricated via 3D printing. One-stroke printing path planning was developed to ensure the continuity of fiber bundles in these auxetic honeycombs. Uniaxial compression tests along two loading directions were conducted to evaluate in-plane mechanical properties. Damage types of the auxetic honeycombs after tests were characterized with scanning electron microscopy (SEM). Subsequently, analytical models were developed and printing path-based finite element (FE) simulations were carried out to investigate the dependence of the in-plane mechanical properties on geometrical parameters.

2. Experimental procedures

2.1. Experimental platform and raw materials

The CFRTPC 3D printer employed to fabricate auxetic honeycombs was acquired from Shaanxi FiberTech Technology Development Co., LTD, China. As shown in Fig. 1(a), the FDM-based equipment consisted mainly of an extrusion head, a control system, a building platform, and a X–Y motion mechanism; more details of the printing technology were referred to Tian et al. [32]. Fig. 1(b) illustrated the working process of the extrusion head that received thermoplastic polymer and continuous fiber to construct an ultra-lightweight CFRTPC auxetic honeycomb (Fig. 1(c)). For the present study, Kevlar R fiber (with linear density of 145 dtex and density of 1440 kg/m^3) from DuPont Corp. was employed as the reinforcement material, and polylactic acid (PLA/1.75 mm, density of 1240 kg/m^3) filament from FLASHFORGE Corp. (China) was used as the thermoplastic material.

2.2. Structure design and 3D printing process

As illustrated in Fig. 2, CFRTPC auxetic honeycomb specimens were constructed using 5×3 unit cells, with geometric dimensions as listed in Table 1. Since flexible fiber cutting and fiber connecting was not introduced into the 3D printing process, only one single continuous fiber bundle was used to print the whole auxetic structure. Therefore, a
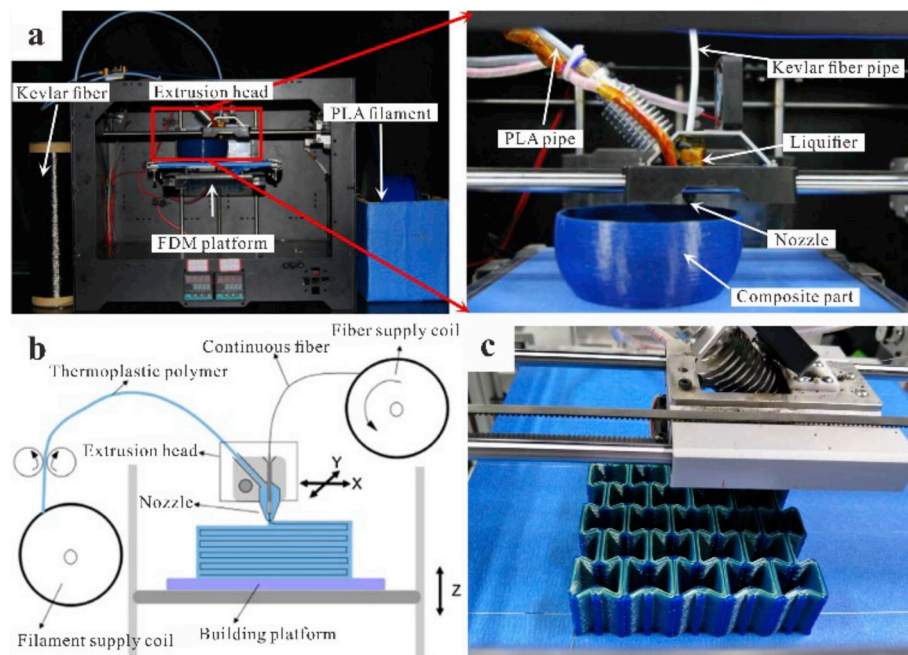

Fig. 1. Equipment and scheme of 3D printing for CFRTPC auxetic honeycombs: (a) setup for 3D printer [32], (b) 3D printing process for CFRTPCs [30], and (c) 3D printing process for CFRTPC auxetic honeycomb.
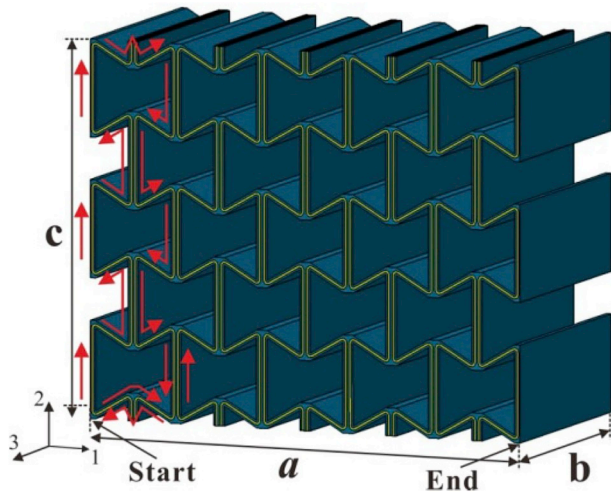
Fig. 2. Schematic of CFRTPC auxetic honeycomb with specific printing path marked in red lines. (For interpretation of the references to colour in this figure legend, the reader is referred to the Web version of this article.)

specific one-stroke printing path was developed as shown in Fig. 2, to ensure the continuity of fiber bundle in the whole printing process. Since the diameter of the Kevlar R fiber is about 12 μm, it is very difficult to simulate the real-size structure across scales from 10 μm to 100 mm. As a simplification, the thermoplastic matrix infiltrated fibers were treated as a whole part (named fiber bundle) at an "intermediate" scale. Based upon the printing continuity, fiber bundle and pure matrix parts were separately taken into account in subsequent analytical modeling and FE simulations. Besides, with the fiber bundle taken as continuous along the 3-direction, plane-strain could be assumed. With reference to Table 1 and Fig. 3, the unit cell of the CFRTPC auxetic honeycomb was characterized by: length of vertical strut h, length of inclined strut l, clockwise angle of inclined strut from horizontal direction θ, whole thickness of vertical strut t_1, whole thickness of inclined strut t_2, thickness of external matrix part of vertical and inclined struts t_m, thickness of internal fiber bundle part of vertical and inclined struts t_f, and thickness of internal matrix part of vertical strut t_{m1}. SEM measurement method was used to obtain the accurate average value of t_m, t_{m1}, t_f, t_1 and t_2. The relative density of the CFRTPC auxetic honeycomb could thence be calculated as:

$$\frac{\rho^*}{\rho_s} = \frac{ht_1 + 2lt_2}{2(l\cos\theta + t_1)(h - l\sin\theta - t_2/\cos\theta)} \tag{1}$$

where ρ^* and ρ_s denoted the densities of unit cell and bulk material (in this case Kevlar fiber reinforced PLA composite material, 1248 kg/m^3) respectively.

During the 3D printing process, the printing parameters were set as: layer thickness of 0.2 mm, hatch spacing of 1 mm, printing speed of 100 mm/min, nozzle temperature of 210 °C, enabling a tradeoff between printing accuracy and efficiency [32]. As shown in Fig. 4, typical printing defects of the present CFRTPC auxetic honeycombs included: (a) for certain inclined struts, the direction of fiber bundles was somewhat deviated from that of the struts; (b) a small amount of fiber bundles were pulled out from the matrix at some corners; (c) pure matrix areas with fiber loss occurred when the direction of printing path changed 180°. These printing defects may influence the mechanical properties of the prismatic structure.

2.3. Material properties

As mentioned in the previous section, the fiber bundle and matrix parts were considered separately in analytical and FE models. However, it had proved difficult to directly measure the mechanical properties of the fiber bundle. Alternatively, the elastic modulus and yield strength of a fiber bundle could be derived using the variant of mixing rule, as:

$$E_f = (E_s - E_m)/v_f + E_m \tag{2}$$

$$\sigma_f = (\sigma_s - \sigma_m)/v_f + \sigma_m \tag{3}$$

where E_f, E_s and E_m were the elastic modulus of the fiber bundle, strut and matrix, respectively. σ_f, σ_s and σ_m were the yield strength of the fiber bundle, strut and matrix, respectively. v_f was the fiber bundle volume fraction of the strut. For the inclined and vertical struts, v_f was calculated as t_f/t_2 and $2t_f/t_1$, respectively.

Uniaxial tensile tests were carried out with hydraulic testing machine (MTS) to measure the basic mechanical properties of the tensile specimen for fiber-reinforced thermoplastic composites, as shown in Fig. 5(a). Extensometer was used to measure strain. Fig. 6 displayed the
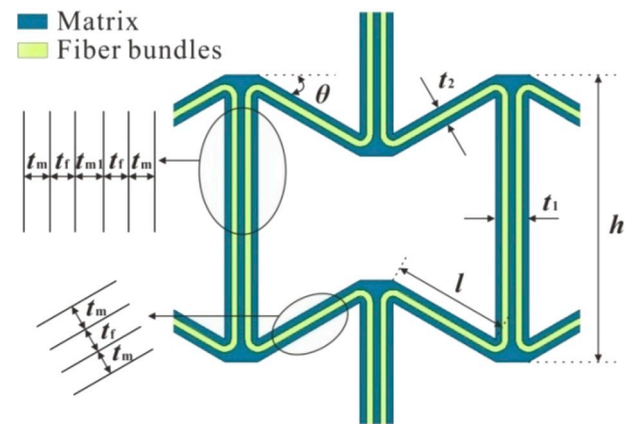

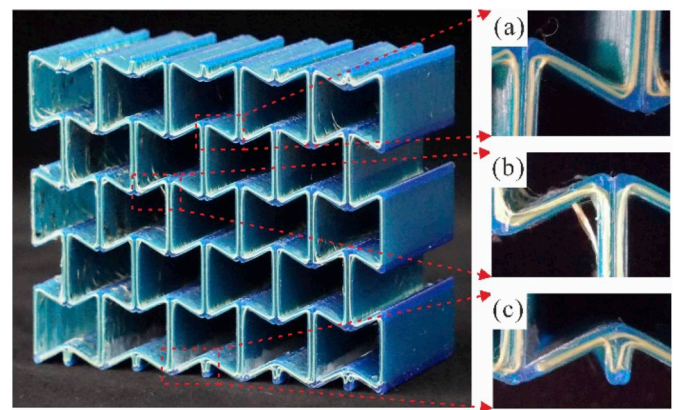**Fig. 3.** Unit cell of CFRTPC auxetic honeycomb.

Fig. 4. The 3D printed CFRTPC auxetic honeycomb with typical printing defects: (a) deviation of the fiber alignment, (b) fiber pullout, and (c) pure matrix area.

Table 1
Geometric parameters of 3D printed CFRTPC auxetic honeycomb (unit: mm).

h	l	t_1	t_2	t_m	t_{m1}	t_f	θ	a	b	c
20.52	8.45	2.36	1.38	0.46	0.52	0.46	30°	96.80	50.00	79.34

measured tensile stress versus strain curves of the inclined struts, vertical struts and 3D printed PLA specimens. Then, together with Eqs. (2) and (3), the elastic modulus and yield strength of the strut, the fiber bundle and the PLA could be calculated; the results were summarized in Table 2. Subsequent FE simulations indicated that using the fiber bundles' properties calculated from the measured inclined struts to simulate all the fiber bundle parts was quite efficient, of which the simulated result was almost the same as that from the case that using the fiber bundles' properties calculated from inclined and vertical struts to simulate inclined and vertical fiber bundle parts, respectively. Consequently, for brevity, the modulus and strength of fiber bundles calculated from inclined struts were employed to characterize all the fiber bundle parts in analytical modeling and FE simulations.

2.4. Mechanical evaluations

The MTS universal testing machine (MTS-880, MTS Corp., U.S.A) was used to perform in-plane compression tests, as shown in Fig. 5(b). With the placement rate fixed at 2 mm/min, a strain up to 60% was achieved to obtain the whole collapse process of CFRTPC auxetic honeycomb at room temperature. The load, displacement and time data were obtained from the machine data acquisition system. The tests were repeated for both horizontal and vertical directions, with each test recorded using a video camera. The nominal stress was defined as the applied force divided by the initial projected cross-sectional area ($b \times c$ when loading along the 1-direction, or $a \times b$ when loading along the 2-direction; see Fig. 2). The nominal axial strain was defined in terms of compression displacement divided by initial height. When loading along the 1-direction, the nominal transverse strain was defined as $\varepsilon_{x1} = (c - x_{n1})/c$, with x_{n1} being the average horizontal distance between opposite marks at the n-th step of loading as shown later in Fig. 11. When loading along the 2-direction, the nominal transverse strain was defined as $\varepsilon_{x2} = (a - x_{n2})/a$, with x_{n2} being the horizontal distance between marks at the n-th step of loading shown in Fig. 14. The Poisson ratio was defined as the negative ratio of the nominal transverse and axial strains.

3. Theoretical model

Under in-plane compression, the struts of a CFRTPC auxetic honeycomb mainly underwent bending and axial stretching. Accordingly, in this section, its elastic modulus and Poisson ratio along the 1- and the 2-
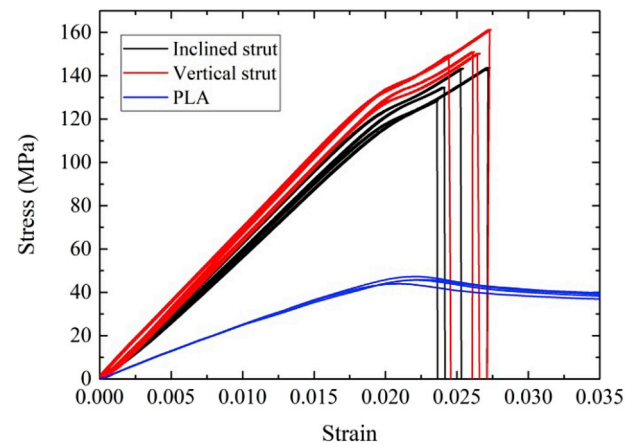
Fig. 6. Measured tensile stress versus strain curves for inclined struts, vertical struts and 3D printed PLA specimens.

Table 2
Mechanical properties of struts, fiber bundles and pure PLA, with the standard deviation depicted in brackets.

Property	Inclined strut	Fiber bundle (calculated from inclined strut)	Vertical strut	Fiber bundle (calculated from vertical strut)	PLA
Modulus, GPa	6.33 (0.16)	13.59 (0.49)	6.90 (0.17)	13.47 (0.44)	2.70 (0.08)
Strength, MPa	140.01 (7.23)	327.63 (21.69)	153.06 (4.53)	320.32 (11.62)	46.20 (1.22)

directions are derived, following the loading scheme as shown in Fig. 7. Symmetrical boundary conditions were applied to ensure the consistency of the expressions of compressive modulus and Poisson ratio between the representative volume element and macroscopic homogeneous.

3.1. Compressing along the 1-direction

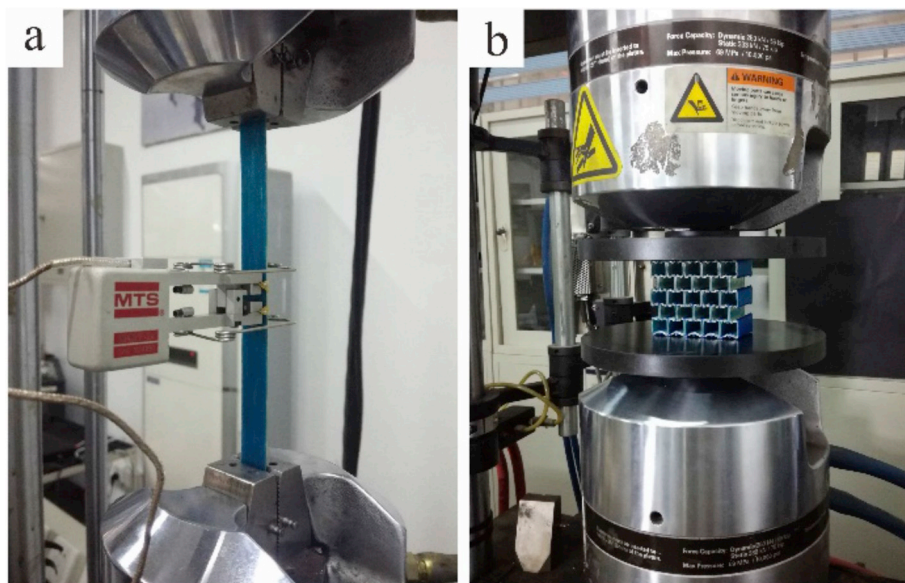When compressed along the 1-direction (Fig. 7(a)), the inclined

Fig. 5. (a) Tensile test for the basic mechanical properties of the tensile specimen for fiber-reinforced thermoplastic composites; (b) compression test for the 3D printed CFRTPC auxetic honeycomb.
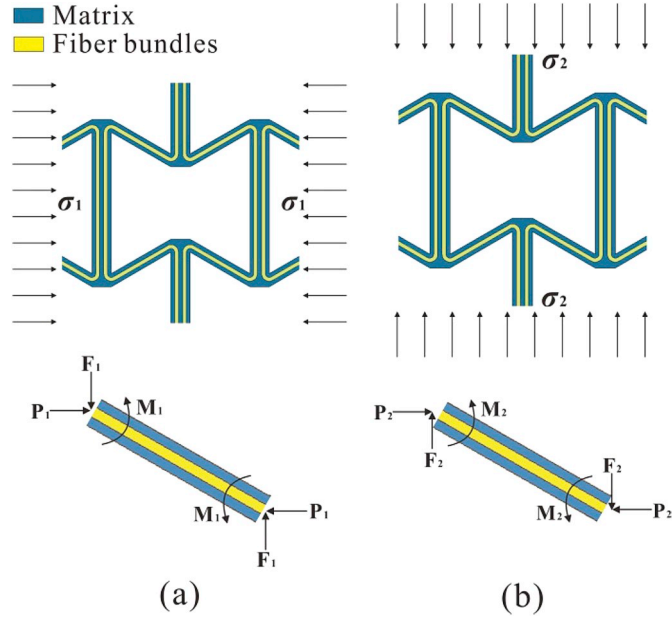
Fig. 7. Top view of unit cell model to calculate in-plane elastic constants: (a) along 1-direction; (b) along 2-direction.

struts were bent and compressed under the nominal compressive stress σ_1. In this case, it had been established that $F_1 = 0$ and $P_1 = \sigma_1 b(h - l\sin\theta - t_2/\cos\theta)$. The moment M_1 tending to bend the inclined strut was calculated using the equilibrium equation, as [42]:

$$M_1 = \frac{1}{2}P_1 l \sin\theta. \tag{4}$$

Then, the bending deflection of the inclined strut was derived based upon the classical beam theory:

$$\delta_{11} = \frac{P_1 l^3 \sin\theta}{12\left(2E_m I_1 + E_f I_2\right)} \tag{5}$$

Here, I_1 and I_2 were the inertia moments of the matrix and fiber bundle parts, respectively, given by:

$$I_1 = \frac{bt_m^3}{12} + \left(\frac{t_m + t_f}{2}\right)^2 t_m b, \quad I_2 = \frac{bt_f^3}{12}. \tag{6}$$

where b was strut width along the 3-direction. Additionally, the inclined strut also bore the axial compressive load component, $P_1\cos\theta$, leading to an extra axial deflection of:

$$\delta_{12} = \frac{P_1 l \cos\theta}{2t_m b E_m + t_f b E_f}. \tag{7}$$

Finally, the total deflection in the 1-direction was obtained as $\delta_{11}\sin\theta + \delta_{12}\cos\theta$, with the corresponding 1-direction compressive strain ε_{11} given by:

$$\varepsilon_{11} = \frac{\delta_{11}\sin\theta + \delta_{12}\cos\theta}{l\cos\theta + t_1}. \tag{8}$$

Thus, the equivalent compressive modulus in the 1-direction was $E_1 = \sigma_1/\varepsilon_{11}$, resulting in:

$$E_1 = \frac{l\cos\theta + t_1}{bl(h - l\sin\theta - t_2/\cos\theta)\left[\frac{l^2 \sin^2\theta}{12\left(2E_m I_1 + E_f I_2\right)} + \frac{\cos^2\theta}{2t_m b E_m + t_f b E_f}\right]}. \tag{9}$$

With the total deflection in the 2-direction given by $\delta_{11}\cos\theta - \delta_{12}\sin\theta$, the 2-direction compressive strain ε_{22} became:

$$\varepsilon_{22} = \frac{\delta_{11}\cos\theta - \delta_{12}\sin\theta}{h - l\sin\theta - t_2/\cos\theta}. \tag{10}$$

Therefore, the Poisson ratio was calculated as $\nu_{12} = -\varepsilon_{22}/\varepsilon_{11}$, giving:

$$\nu_{12} = -\frac{\sin 2\theta\left[\frac{l^2}{12\left(2E_m I_1 + E_f I_2\right)} - \frac{1}{2t_m b E_m + t_f b E_f}\right](l\cos\theta + t_1)}{2\left[\frac{l^2 \sin^2\theta}{12\left(2E_m I_1 + E_m I_2\right)} + \frac{\cos^2\theta}{2t_m b E_m + t_f b E_f}\right](h - l\sin\theta - t_2/\cos\theta)}. \tag{11}$$

3.2. Compressing along the 2-direction

For compressing along the 2-direction as shown in Fig. 7(b), the inclined struts were bent and stretched by the nominal compressive stress σ_2. Similar to the previous case, it was established that $P_2 = 0$, $F_2 = \sigma_2 b(l\cos\theta + t_1)$, and $M_2 = \frac{1}{2}F_2 l \cos\theta$. The bending deflection of the inclined strut was thus calculated as:

$$\delta_{21} = \frac{F_2 l^3 \cos\theta}{12\left(2E_m I_1 + E_f I_2\right)}. \tag{12}$$

The inclined strut also bore an axial tensile load $F_2\sin\theta$, causing an axial tensile deflection of:

$$\delta_{22} = \frac{F_2 l \sin\theta}{2t_m b E_m + t_f b E_f}. \tag{13}$$

The axial deflection of the vertical strut was:

$$\delta_{23} = \frac{2F_2 h}{(2t_m + t_{m1})b E_m + 2t_f b E_f}. \tag{14}$$

Thus, with the total deflection in the 2-direction given by $\delta_{21}\cos\theta + \delta_{22}\sin\theta + \delta_{23}$, the 2-direction nominal strain was:

$$\varepsilon_{22} = \frac{\delta_{21}\cos\theta + \delta_{22}\sin\theta + \delta_{23}}{(h - l\sin\theta - t_2/\cos\theta)}. \tag{15}$$

The equivalent compressive modulus along the 2-direction was $E_2 = \sigma_2/\varepsilon_{22}$, giving:

$$E_2 = \frac{h - l\sin\theta - t_2/\cos\theta}{b(l\cos\theta + t_1)\left[\frac{l^3 \cos^2\theta}{12\left(2E_m I_1 + E_f I_2\right)} + \frac{l\sin^2\theta}{2t_m b E_m + t_f b E_f} + \frac{2h}{(2t_m + t_{m1})b E_m + 2t_f b E_f}\right]}. \tag{16}$$

With the total deflection in the 1-direction given by $\delta_1\sin\theta - \delta_2\cos\theta$, the 1-direction nominal strain was:

$$\varepsilon_{21} = \frac{\delta_1\sin\theta - \delta_2\cos\theta}{l\cos\theta + t_1}. \tag{17}$$

Finally, the Poisson ratio was $\nu_{21} = -\varepsilon_{21}/\varepsilon_{22}$, giving:

$$\nu_{21} = -\frac{l\sin 2\theta\left[\frac{l^2}{12\left(2E_m I_1 + E_f I_2\right)} - \frac{1}{2t_m b E_m + t_f b E_f}\right](h - l\sin\theta - t_2/\cos\theta)}{2\left[\frac{l^3 \cos^2\theta}{12\left(2E_m I_1 + E_f I_2\right)} + \frac{l\sin^2\theta}{2t_m b E_m + t_f b E_f} + \frac{2h}{(2t_m + t_{m1})b E_m + 2t_f b E_f}\right](l\cos\theta + t_1)}. \tag{18}$$

4. Finite element modeling

In-plane compressive behaviors of CFRTPC auxetic honeycombs were modeled using the explicit version of the commercial FE software package, ABAQUS (version 6.14-1). The honeycomb structure was sandwiched between two rigid surfaces simulating the platens of the MTS-880 testing machine as shown in Fig. 8. To mimic both small and large deformations, a printing path-based FE model was developed, which took into account the fiber bundle and pure matrix parts separately. Geometric dimensions of the model and material properties of both the matrix and fiber bundle parts were the same as those given in Section 2. The matrix was treated as isotropic and the plastic properties

measured by experiments were input into ABAQUS via a table. For simplicity, fiber bundle was treated as isotropic and perfectly elastoplastic.

The matrix and fiber bundle parts were meshed with eight noded hexahedral linear element (C3D8R) employing reduced integration. Mesh convergence study showed that the average element size of $t_1/10$ gave efficiently accurate results. Loading velocity sensitivity study showed that 0.5 mm/ms gives a converged solution. The interaction property for contact was applied as ALLWITH SELF with a tangential behavior and friction coefficient penalty of 0.2 to prevent self-penetration of elements. Co-node connection was used between the fiber bundle and matrix parts. When loaded along the 2-direction, all degrees of freedom (translational and rotational) on the bottom rigid surface and rotational degrees of freedom on the top rigid surface were constrained. A displacement control boundary was applied on the top rigid surface. Similar settings of FE simulations were adopted for compressing along the 1-direction.

5. Results and discussion

5.1. Compressive behaviors

Fig. 9 compared the FE predicted nominal compressive stress–strain responses for both CFRTPC and pure PLA auxetic honeycombs with experimental measurements when compressive loading applied along the 1-direction. Deformation mechanisms corresponding to the numbered bullet markers on the response curve were displayed in Fig. 11. Overall, good agreement was achieved between experiments and simulations, confirming the fidelity of the present FE modelling. Under in-plane compression along the 1-direction, uniformly linear and small elastic deformation of the auxetic honeycomb started from configuration ①. The first peak stress in Fig. 9 was reached at configuration ②, followed by a sudden drop, which was attributed to the instability and printing defects of the struts. As the structure was further compressed from ② to ③, the deformation was gradually localized in the form of rotating inclined struts, corresponding to a short stress plateau with small fluctuations. From ③ to ⑤, localized densification formed layer by layer in an asymmetric way. Correspondingly, the nominal stress increased with some fluctuations as shown in Fig. 9. As the CFRTPC auxetic honeycomb was compressed to configuration ⑥, densification of the whole structure was achieved, corresponding to the maximum of stress on the stress-strain curve.

Fig. 10 plotted the Poisson ratio ν_{12} as a function of the nominal strain for both CFRTPC and pure PLA auxetic honeycombs when loaded along the 1-direction. The Poisson ratio increased with increasing compressive strain. During the whole loading process, the auxetic honeycomb exhibited a negative Poisson ratio, which was smaller than that of the pure PLA structure.
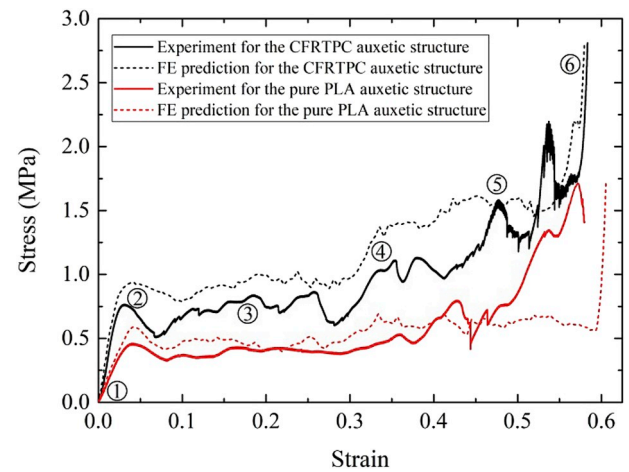

Fig. 9. Compressive stress versus strain responses of CFRTPC and pure PLA auxetic honeycombs under 1-direction compression: comparison between experiments and FE simulations.

Fig. 12 compared the numerically predicted nominal compressive stress–strain responses of both CFRTPC and pure PLA auxetic honeycombs with experimental measurements for the case of loading along
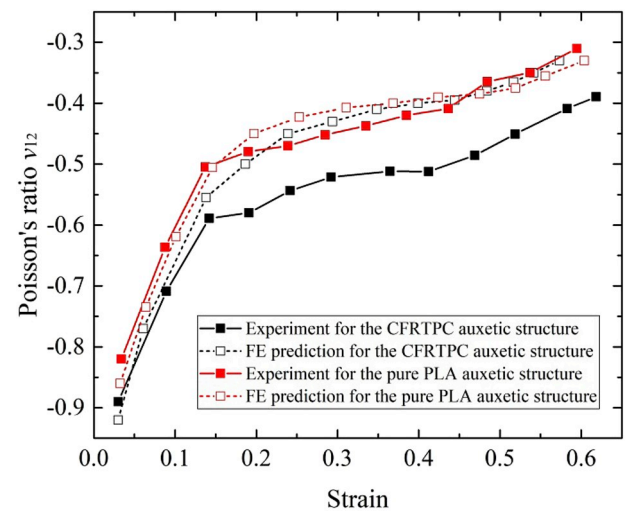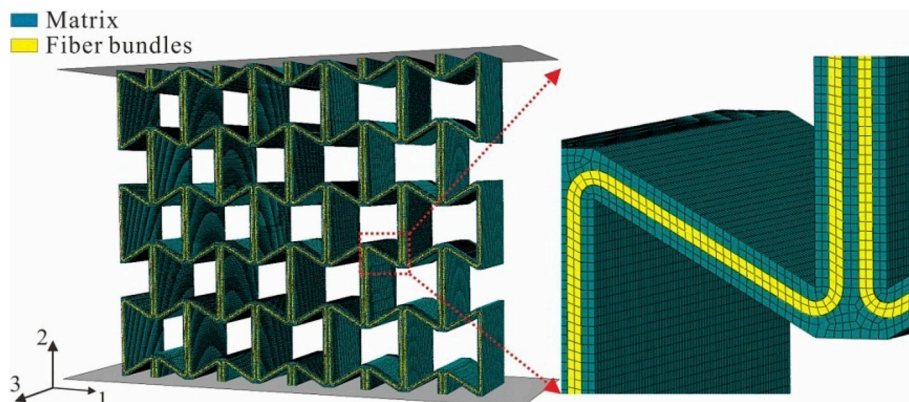

Fig. 10. Poisson ratio ν_{12} versus strain responses of CFRTPC and pure PLA auxetic honeycombs under 1-direction compression: comparison between experiments and FE simulations.

Fig. 8. Details of the FE model for compressing along the 2-direction.
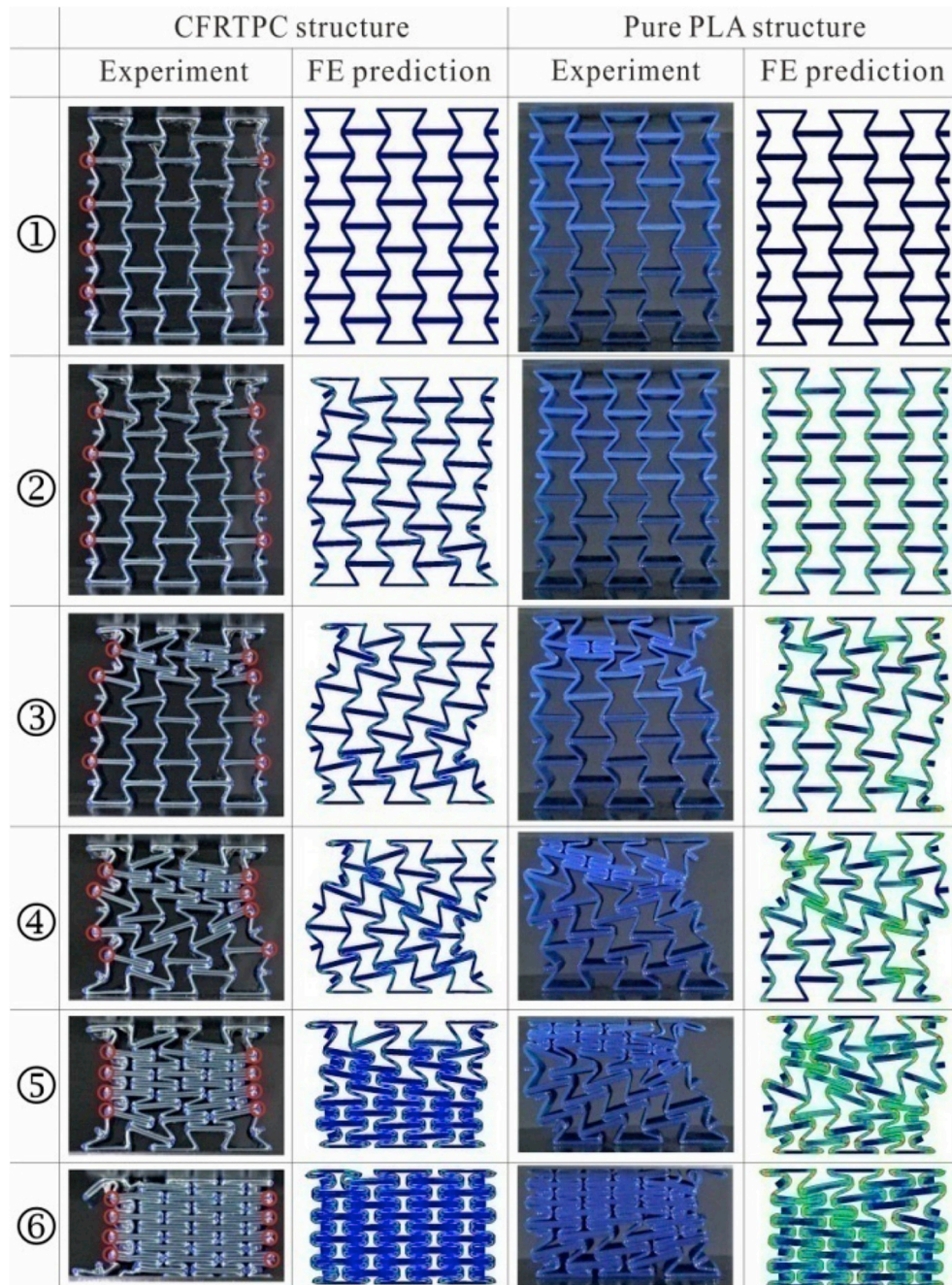
Fig. 11. Comparsion of exprimentally observed and FE simulated deformation configurations for both CFRTPC and pure PLA auxetic honeycombs subjected to 1-direction in-plane compression. The numbers corresponded to different loading stages as shown in Fig. 9.

the 2-direction. Deformation mechanisms corresponding to the numbered bullet markers on the response curve were displayed in Fig. 14. Again, good agreement between experiments and FE predictions was achieved. As the structure was compressed from configuration ② to ☐, the vertical struts of the same row rotated in the same direction while adjacent rows rotated in opposite directions, resulting in a long stress plateau. From ③ to ⑤, the vertical struts of adjacent rows gradually came into contact with each other, leading to an upward stress trajectory. From ④ to ⑤, a multitude of cracks were formed in the matrix. Correspondingly, the stress-train curve entered a nearly stress stagnant region with lots of small fluctuations as shown in Fig. 12. Different from the case of 1-direction compression, the stress exhibited multi-plateau effect during the whole process. For the pure PLA structure, the struts broke when the nominal strain reached 0.45, which caused a sudden

decrease of the carrying capacity. In contrast, the continuous fibers prohibited efficiently the propagation of cracks in the matrix for each ligament, thus preventing the breakage of struts and the structure from being crushed as shown in Fig. 14.

Fig. 13 plotted the Poisson ratio ν_{21} as a function of nominal strain for both CFRTPC and pure PLA auxetic honeycombs when loaded along the 2-direction. Different from the case of 1-direction compression, ν_{21} first decreased and then increased, leading to a minimum value when the strain was 0.17; it then changed from negative to positive when the strain was increased to 0.52. Again, the Poisson ratio of the CFRTPC structure was smaller than that of the pure PLA structure.

The in-plane properties of the present CFRTPC auxetic honeycombs obtained from experiments, FE simulations and analytical predictions were compared in Table 3. Overall, the good agreement validated the
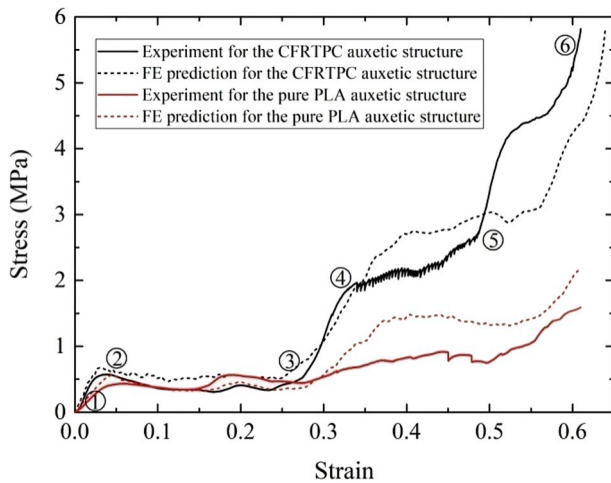
Fig. 12. Compressive stress versus strain responses of CFRTPC and pure PLA auxetic honeycombs under 2-direction compression: comparison between experiments and FE simulations.
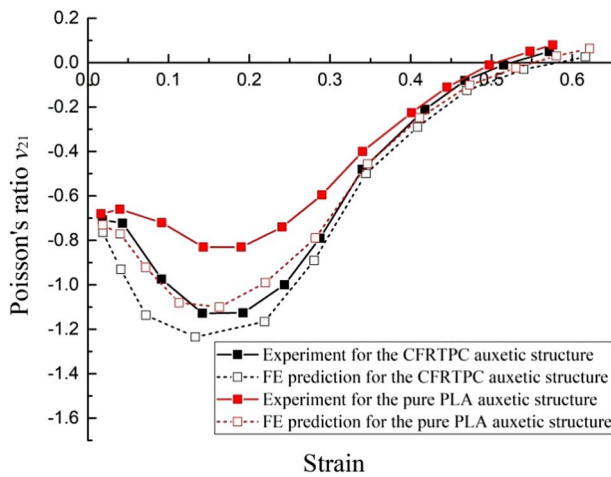

Fig. 13. Poisson ratio ν_{21} versus strain responses of CFRTPC and pure PLA auxetic honeycombs under 2-direction compression: comparison between experiments and FE simulations.

effectiveness of the printing path-based FE method and the analytical model. Nonetheless, the slightly large deviation of Poisson ratio between the experiments and analytical predictions might be induced by the printed defects and limited image resolution for local deformation during image processing.

Table 4 compared the in-plane properties of CFRTPC and pure PLA auxetic honeycombs. Energy absorption was calculated by integrating the nominal stress-strain cueves up to the nominal strain of 0.5:

$$W = \int_0^{0.5} \sigma(\varepsilon)d\varepsilon \qquad (19)$$

The CFRTPC structure exhibited considerable advantages in terms of in-plane mechanical properties compared to the pure PLA structure. With the addition of continuous fibers, the mass was increased only by 6%, but the Poisson ratio was reduced; further, the 1-direction compressive stiffness, the 2-direction compressive stiffness, the 1-direction energy absorption, and the 2-direction energy absorption were dramatically increased by 98.7%, 86.3%, 87% and 100%, respectively.

5.2. Damage types

After the in-plane compression test, damage types in CFRTPC honeycomb were observed with the help of SEM images, as shown in Fig. 15(a–d). At a certain level of the compressive load, cracks initiated from the edge of the matrix at some corners, and propagated along the cross-section until it met with the fibers. The propagation of cracks in the matrix was prohibited by the fiber bundles, attributed to the high strength of the Kevlar fibers. Afterwards, a few local interfacial debondings occurred due to the high shear stress in the interface region between fiber and matrix, which led to subtle crack propagation. Then, a few fibers were pulled out from matrix due to their high fracture elongation (3.6%) and consumed some energy by friction. Meanwhile, the fibers moderately eased the stress concentration at the crack tips of the matrix. When densification of the CFRTPC auxetic honeycomb was achieved, there was not enough force to break the fibers and the equilibrium was reached at the crack region. In this way, the continuous fibers prohibited the propagation of cracks in the matrix, thus preventing the breakage of struts and the fracture of the structure, as shown in Fig. 15(a). When the nominal strain exceeded 0.3, delamination occurred between adjacent deposited lines, mainly attributed to the relatively poor bonding strength and the large tension on both sides of the vertical strut provided by the inclined struts under the 2-direction compression, as shown in Fig. 15(b). No delamination was observed during the entire process of the 1-direction compression for the vertical struts mainly subjected to transverse compressive loads when the structure was greatly deformed. Due to the lack of fiber reinforcement, fractures occurred in certain pure matrix areas (see Fig. 15(c)), as a result of the printing defects as described in Section 2. When loaded along the 2-direcion, as the angle between inclined and vertical struts gradually increased, the local interfacial debonding was observed between fiber and matrix caused by transverse stretching at certain corners, with voids formed, as shown in Fig. 15(d). Again, no void was observed for the angle between inclined and vertical struts decreased during the entire process of the 1-direction compression. For comparison, the complete cross-sectional morphology of the fractured struts in pure PLA structure was presented in Fig. 15(e). Due to the lack of sufficient pressure in the printing process, visible voids were formed at the interface of each pair of adjacent layers, which might reduce the mechanical properties of the structure.

5.3. Parametric study

The CFRTPC auxetic honeycomb had a re-entrant hexagonal section that produced in-plane compression stiffness similar to the one described by the Gibson-Ashby model for classical center-symmetric hexagonal configurations [42]. The sensitivity of its in-plane stiffness and Poisson ratio to variations in geometric parameters could be identified by performing parameter analysis from Eqs. ((9), (11), (16) and (18). Subsequently, for all the calculations, the parameters of t_1/l and t_2/l were set as 0.28 and 0.16, respectively.

Figs. 16 and 17 plotted the FE homogenization and analytical predictions of the in-plane compression modulus E_1 and Poisson ratio ν_{12} as functions of cell angles for selected values of h/l, respectively. As shown in both figures, there was good agreement between FE homogenization and analytical predictions. The results of Fig. 16 showed that E_1 decreased with increasing h/l while other parameters remained constant. Besides, it increased in an increasingly faster manner as the cell angle approached 0°, either from positive or negative. Fig. 17 indicated that when the cell angle was negative, the Poisson ratio ν_{12} was positive, and increased first and then decreased with the increase of cell angle. This led to a maximum value of ν_{12} when the cell angle was about −6°. For positive cell angles, ν_{12} was negative, and decreased first and then increased with the increase of cell angle, resulting in a minimal ν_{12} when the cell angle was about −7°. Moreover, ν_{12} decreased as h/l was increased when the cell angle was negative, but increased with
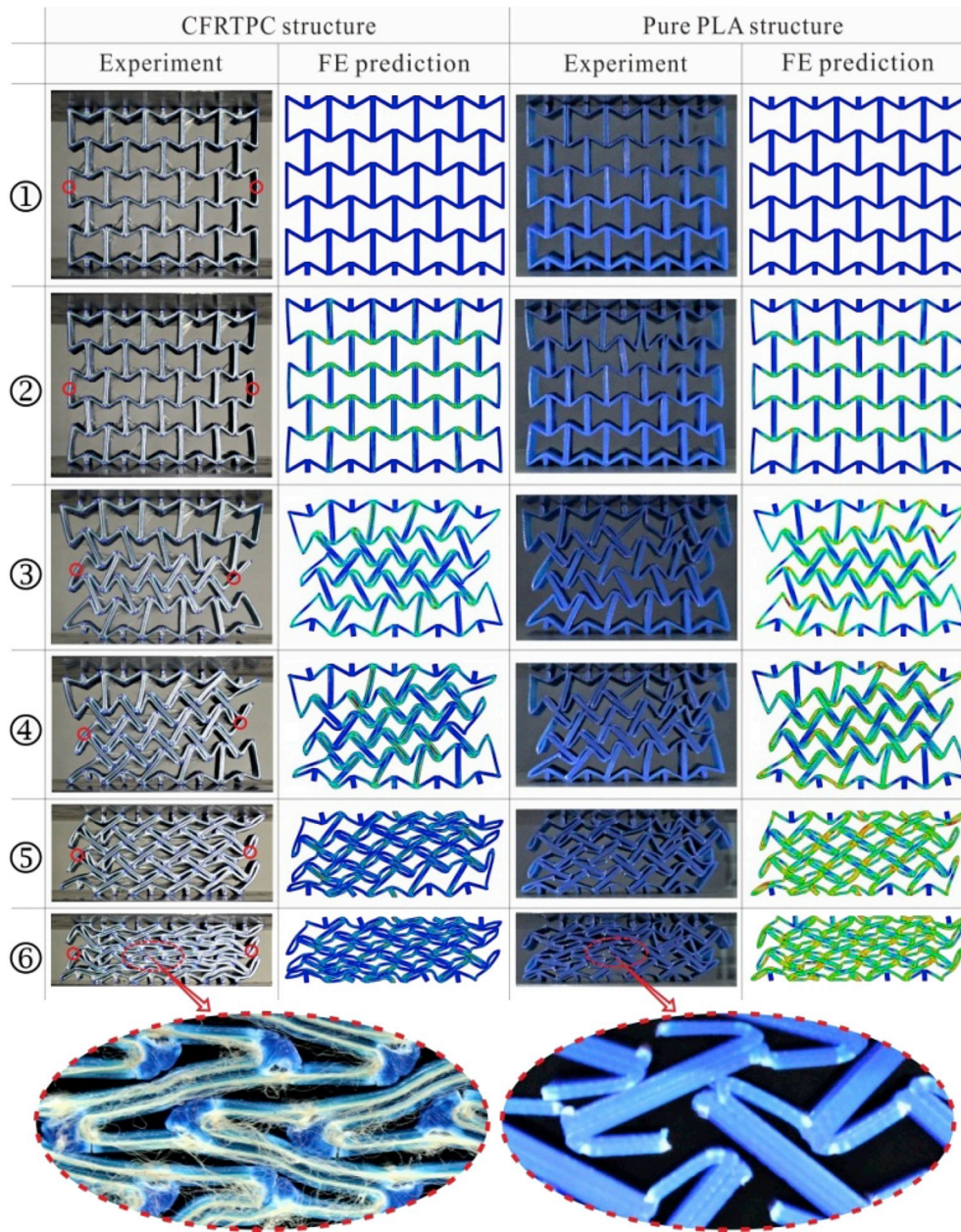
Fig. 14. Comparsion of exprimentally observed and FE calculated deformation configurations for the CFRTPC and pure PLA auxetic honeycombs under the 2-direction in-plane compression. The numbers are corresponding to different loading stages as shown in Fig. 12.

Table 3
Comparison of in-plane properties of CFRTPC auxetic honeycomb, with the standard deviation depicted in brackets.

	Compression Modulus, E_1 (MPa)	Error, δ_{E1} (%)	Poisson ratio, ν_{12}	Error, $\delta\nu_{12}$ (%)	Compression Modulus, E_2 (MPa)	Error, δ_{E2} (%)	Poisson ratio, ν_{21}	Error, $\delta\nu_{21}$ (%)
Experiment	31.95(1.08)		−0.89(0.03)		24.85(0.97)		−0.71(0.02)	
FE simulation	34.02	6.48	−0.92	3.37	25.95	4.43	−0.76	7.04
Analytical prediction	34.25	7.2	−1.08	21.35	26.09	4.99	−0.82	15.49

increasing h/l when the cell angle was positive.

In Figs. 18 and 19, the FE homogenization and analytical predictions of compression modulus E_2 and Poisson ratio ν_{21} and their dependence on cell angle for selected values of h/l were presented. The FE homogenization and analytical predictions of the Poisson ratio showed excellent agreement but diviated somewhat for the compression modulus. The compression modulus first decreased and then increased with increasing cell angle, taking a minimum value when the cell angle was

about 10° (Fig. 17). In addition, it increased as h/l was increased while other geometrical parameters remained constant. Fig. 19 illustrated that ν_{21} was positive when the cell angle was negative, and negative when the cell angle was positive. It decreased with increasing cell angle. Further, ν_{21} increased with increasing h/l when cell angle was negative and decreased with increasing h/l when cell angle was positive.

Table 4

Comparison of in-plane properties between CFRTPC and pure PLA auxetic honeycombs, with the standard deviation depicted in brackets.

	Loading along the 1-direction			Loading along the 2-direction			Weight (g)
	Compression Modulus, E_1 (MPa)	Poisson ratio, ν_{12}	Energy absorption ($\times 10^6$ J/m^3)	Compression Modulus, E_2 (MPa)	Poisson ratio, ν_{21}	Energy absorption ($\times 10^6$ J/m^3)	
CFRTPC	31.95(1.08)	−0.89(0.03)	0.43(0.01)	24.85(0.97)	−0.71(0.02)	0.56(0.02)	123(2)
Pure PLA	16.08(0.52)	−0.82(0.02)	0.23(0.01)	13.34(0.36)	−0.68(0.02)	0.28(0.01)	116(2)
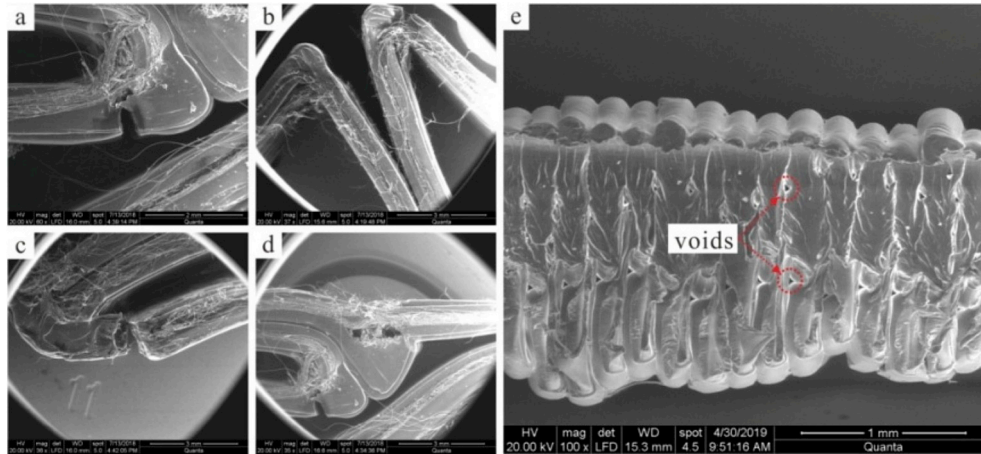
Fig. 15. SEM images showing various damage types: (a) crack, (b) delamination, (c) fracture, and (d) void in CFRTPC auxetic honeycomb after test; (e) cross-sectional morphology of fractured struts in pure PLA auxetic honeycomb after test.
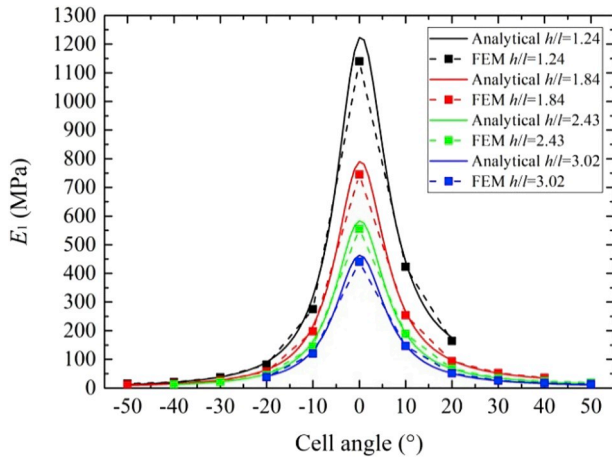
Fig. 16. Effect of cell angle on compressive modulus E_1 for selected values of h/l with $t_1/l = 0.28$ and $t_2/l = 0.16$.
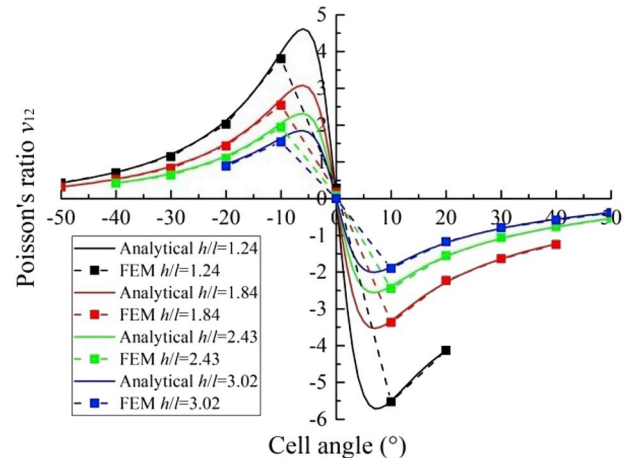

Fig. 17. Effect of cell angle on Poisson ratio ν_{12} for selected values of h/l with $t_1/l = 0.28$ and $t_2/l = 0.16$.

6. Conclusions

This study demonstrates the low-cost rapid manufacturing of CFRTPC auxetic honeycomb structures using 3D printing technology, and a convenient one-stroke printing path planning was developed. A combined experimental, analytical and numerical approach was employed to investigate the in-plane compressive behaviors of CFRTPC auxetic honeycombs. The main findings were summarized as follows:

(1) The printing path-based analytical model and FE method took into account both the fiber bundle and pure matrix parts and hence were reliable for the design of 3D printed continuous FRCLSs.

(2) In contrast to pure PLA structures, CFRTPC auxetic honeycombs had smaller Poisson ratios and exhibited dramatic increase of the 1-direction compressive stiffness, the 2-direction compressive stiffness, the 1-direction energy absorption, and the 2-direction energy absorption by 98.7%, 86.3%, 87% and 100%, respectively, while the mass was increased only by 6%.

(3) For CFRTPC auxetic honeycombs, the continuous fibers prohibited efficiently the propagation of cracks in the matrix, which in turn prevented the breakage of struts and the whole structure from being crushed. In contrast, the struts fractured prematurely for pure PLA structures, leading to a sudden drop in load.

(4) Large variations and control of in-plane mechanical properties can be tailored by altering unit cell geometric parameters for CFRTPC auxetic honeycombs.
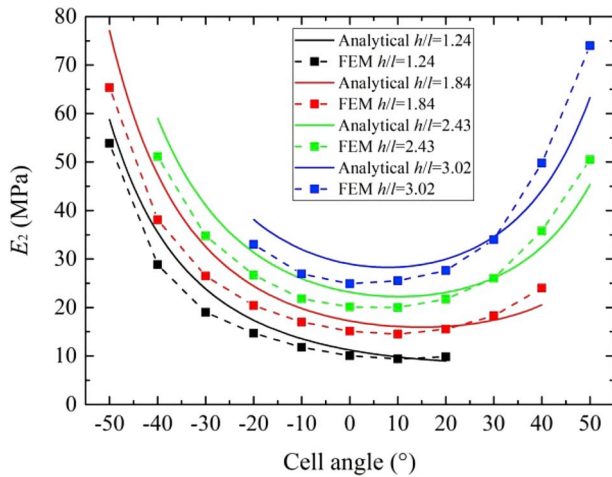
Fig. 18. Effect of cell angle on compressive modulus E_2 for selected values of h/l with $t_1/l = 0.28$ and $t_2/l = 0.16$.
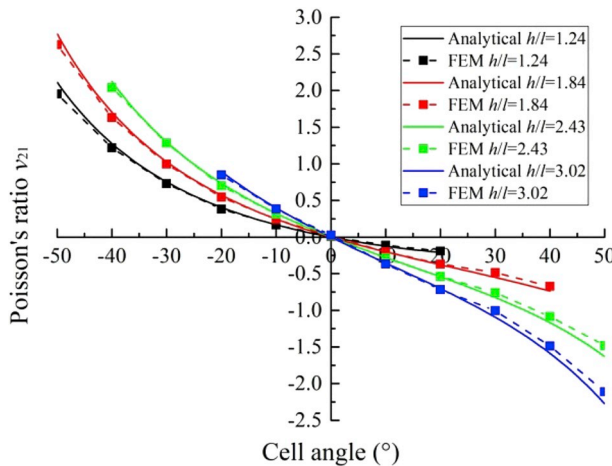

Fig. 19. Effect of cell angle on Poisson ratio ν_{21} for selected values of h/l with $t_1/l = 0.28$ and $t_2/l = 0.16$.

(5) The mechanical properties of CFRTPC auxetic honeycombs can be further improved by increasing the fiber content and reducing the printing defects.

Declaration of competing interest

The authors declare that they have no known competing financial interests or personal relationships that could have appeared to influence the work reported in this paper.

Acknowledgement

References

[1] Bitzer T. Honeycomb technology: materials, design, manufacturing, applications and testing. Springer; 1997.

[2] Lakes R. Foam structures with a negative Poisson's ratio. Science 1987;235: 1038–41.

[3] Friis EA, Lakes RS, Park JB. Negative Poisson's ratio polymeric and metallic foams. J Mater Sci 1988;23(12):4406–14.

[4] Loureiro MA, Lakes RS. Scale-up of transformation of negative Poisson's ratio foam: Slabs. Cell Polym 1997;16(5):349–63.

[5] Caddock BD, Evans KE. Microporous materials with negative Poisson's ratios. I. Microstructure and mechanical properties. J Phys D Appl Phys 1989;22(12):1877.

[6] Alderson KL, Kettle AP, Neale PJ, et al. The effect of the processing parameters on the fabrication of auxetic polyethylene. J Mater Sci 1995;30(16):4069–75.

[7] Alderson KL, Alderson A, Davies PJ, et al. The effect of processing parameters on the mechanical properties of auxetic polymeric fibers. J Mater Sci 2007;42(19): 7991–8000.

[8] Milton GW. Composite materials with Poisson's ratios close to - 1. J Mech Phys Solid 1992;40(5):1105–37.

[9] Hine PJ, Duckett RA, Ward IM. Negative Poisson's ratios in angle-ply laminates. J Mater Sci Lett 1997;16(7):541–4.

[10] Alderson KL, Alderson A, Smart G, et al. Auxetic polypropylene fibres: Part 1-Manufacture and characterization. Plast Rubber Compos 2002;31(8):344–9.

[11] Alderson KL, Simkins VR, Coenen VL, et al. How to make auxetic fibre reinforced composites. Phys Status Solidi 2010;242(3):509–18.

[12] Alderson A, Alderson KL. Auxetic materials. J Aero Eng 2007;221(4):565–75.

[13] Lorato A, et al. The transverse elastic properties of chiral honeycombs. Compos Sci Technol 2010;70(7):1057–63.

[14] Hou Y, et al. Graded conventional-auxetic Kirigami sandwich structures: flatwise compression and edgewise loading. Compos B Eng 2014;59:33–42.

[15] Huang J, et al. In-plane elasticity of a novel auxetic honeycomb design. Compos B Eng 2017;110:72–91.

[16] Li T, Wang L. Bending behavior of sandwich composite structures with tunable 3D-printed core materials. Compos Struct 2017;175:46–57.

[17] Imbalzano G, et al. Blast resistance of auxetic and honeycomb sandwich panels: comparisons and parametric designs. Compos Struct 2018;183:242–61.

[18] Jiang Y, Li Y. 3D printed auxetic mechanical metamaterial with chiral cells and re-entrant cores. Sci Rep 2018;8(1):2397.

[19] Wang XT, Li XW, Ma L. Interlocking assembled 3D auxetic cellular structures. Mater Des 2016;99:467–76.

[20] Li Y, et al. Compressive properties of Ti–6Al–4V auxetic mesh structures made by electron beam melting. Acta Mater 2012;60(8):3370–9.

[21] Wang K, et al. Designable dual-material auxetic met materials using three-dimensional printing. Mater Des 2015;67:159–64.

[22] Imbalzano G, et al. A numerical study of auxetic composite panels under blast loadings. Compos Struct 2016;135:339–52.

[23] Wang XT, Chen YL, Ma L. The manufacture and characterization of composite three-dimensional re-entrant auxetic cellular structures made from carbon fiber reinforced polymer. J Compos Mater 2018;52(23):3265–73.

[24] Finnegan KA. Carbon fiber composite pyramidal lattice structures[D]. University of Virginia; 2007.

[25] Lee BC, et al. The compressive response of new composite truss cores. Compos B Eng 2012;43(2):317–24.

[26] Wang B, et al. Mechanical behavior of the sandwich structures with carbon fiber-reinforced pyramidal lattice truss core. Mater Des 2010;31(5):2659–63.

[27] Zhang GQ, et al. Mechanical behavior of CFRP sandwich structures with tetrahedral lattice truss cores. Compos B Eng 2012;43(2):471–6.

[28] Jishi HZ, Umer R, Cantwell WJ. The fabrication and mechanical properties of novel composite lattice structures. Mater Des 2016;91:286–93.

[29] Quan ZZ, et al. Additive manufacturing of multi-directional performs for composites: opportunities and challenges. Mater Today 2015;18(9):503–12.

[30] Yang CC, et al. 3D printing for continuous fiber reinforced thermoplastic composites: mechanism and performance. Rapid Prototyp J 2017;23(1):209–15.

[31] Matsuzaki R, et al. Three-dimensional printing of continuous-fiber composites by in-nozzle impregnation. Sci Rep 2016;6:23058.

[32] Tian XY, et al. Interface and performance of 3D printed continuous carbon fiber reinforced PLA composites. Compos Part A-Appl S 2016;88:198–205.

[33] Li NY, Li YG, Liu ST. Rapid prototyping of continuous carbon fiber reinforced polylactic acid composites by 3D printing. J Mater Process Technol 2016;238: 218–25.

[34] Dickson AN, et al. Fabrication of continuous carbon, glass and Kevlar fiber reinforced polymer composites using additive manufacturing. Addit. Manuf. 2017; 16:146–52.

[35] Caminero M, Chacón J, García-Moreno I, Reverte J. Interlaminar bonding performance of 3D printed continuous fibre reinforced thermoplastic composites using fused deposition modelling. Polym Test 2018;68:415–23.

[36] Caminero M, Chacón J, García-Moreno I, Rodríguez G. Impact damage resistance of 3D printed continuous fibre reinforced thermoplastic composites using fused deposition modelling. Compos B Eng 2018;148:93–103.

[37] Chacón J, Caminero M, Núñez P, García-Plaza E, García-Moreno I, Reverte J. Additive manufacturing of continuous fibre reinforced thermoplastic composites using fused deposition modelling: effect of process parameters on mechanical properties. Compos Sci Technol 2019:107688.

[38] Yamawaki M, Yousuke K. Fabrication and mechanical characterization of continuous carbon fiber-reinforced thermoplastic using a perform by three-dimensional printing and via hot-press molding. Adv Compos Mater 2017:1–11.